




## Spatiotemporal coupled-mode theory for Fabry-Pérot resonators and its application to linear variable filters

Dmitry A. Bykov , Evgeni A. Bezus , and Leonid L. Doskolovich \*

*Samara National Research University, 34 Moskovskoye shosse, Samara 443086, Russia*  
*and Image Processing Systems Institute, National Research Centre “Kurchatov Institute”, 151 Molodogvardeyskaya st., Samara 443001, Russia*



(Received 16 May 2024; accepted 22 July 2024; published 12 August 2024)

Coupled-mode theory (CMT) is a widely used approach for describing resonances and eigenmodes in various photonic structures. Here, we propose a formulation of the CMT describing resonant multilayer structures. In particular, we revisit the conventional Fabry-Pérot resonator and describe its optical properties from the point of view of the spatiotemporal formulation of the CMT. This formulation provides partial differential equations describing both temporal and spatial evolution of the field distribution, thus generalizing the conventional temporal and spatial versions of the CMT. The developed CMT takes into account the symmetry of the considered structure, energy conservation law, reciprocity, and causality. By considering the parameters of the developed CMT to be spatially dependent, we apply it to describe the optical properties of linear variable filters (LVFs) comprising two Bragg mirrors separated by a wedge-shaped (tapered) layer. In good agreement with the results of the rigorous numerical solution of Maxwell’s equations, the proposed CMT accurately reproduces the broadening of the resonant peak and the appearance of Fizeau fringes when increasing the wedge angle of the LVF.

DOI: [10.1103/PhysRevA.110.023511](https://doi.org/10.1103/PhysRevA.110.023511)

### I. INTRODUCTION

Coupled-mode theory (CMT) is an efficient analytical tool for describing resonant optical properties of various photonic structures. Usually, either the temporal or spatial formulation of the CMT is used. Temporal CMT considers the amplitude of the eigenmode to be a function of time [1–3]. In contrast, spatial CMT describes how the field amplitude changes in space [1,4–7].

Recently, considerable interest was drawn to the development of different versions of the so-called spatiotemporal CMT, which is formulated as a partial differential equation (PDE) for the mode amplitude considered as a function of both spatial and temporal variables [8–15]. In particular, in [8,9], the authors studied the spatiotemporal mode coupling in a system of parallel waveguides, the dielectric function of which can also be time dependent. In papers [10,11], a spatiotemporal CMT was formulated for a dispersive medium undergoing a spatiotemporal perturbation. In papers [12,13] by the present authors, the spatiotemporal CMT was presented to describe resonances in guided-mode resonant gratings supporting bound states in the continuum. In [14], a spatiotemporal CMT was used to describe temporal waveguide coupling. In a recent paper [15], a spatiotemporal CMT was developed to describe nonlocal metasurfaces.

In this work, we develop a spatiotemporal CMT for a Fabry-Pérot resonator in a symmetric environment. The presented approach allows us to obtain two similar CMT formulations, both satisfying the energy conservation law and

reciprocity. The first CMT formulation assumes the scattering amplitude to be an even function of the angular frequency  $\omega$ , whereas the second one considers Hermitian functions. We show that the second approach allows the CMT to satisfy the causality condition. Importantly, the parameters of the developed CMT are expressed through the “local” reflection and transmission coefficients of the resonator claddings, so that no overlap integrals are required to be calculated for finding the coupling coefficients featured in the CMT.

The fact that the parameters of the proposed CMT analytically depend on the thickness of the resonator makes it possible to extend the developed theory to the structures, in which this thickness is a spatially varying function. A practically important case of such structures, which we consider in the current work, is a Fabry-Pérot resonator with a *linearly* varying thickness. Such structures are usually referred to as linear variable filters (LVFs) since the filtered wavelength changes almost linearly along the structure. Due to this property, LVFs are widely used in microspectrometers [16–20], optical sensors [21,22], and hyperspectral imaging systems [23–25]. For the considered example of an LVF with Bragg mirror claddings, we demonstrate that the predictions of the developed CMT with varying parameters are in good agreement with the results of electromagnetic simulations based on the rigorous coupled-wave analysis (RCWA) technique [26].

The paper is organized as follows. In Sec. II, we describe the geometry of the considered diffraction problem, introduce the used notation, and discuss several important facts about the Fabry-Pérot interferometer necessary for the further derivations. Sections III and IV present the derivation of the two proposed CMT formulations. In Sec. V, we apply the

\*Contact author: leonid@ipsiras.ru

developed CMT to describe the optical properties of an LVF. Section VI concludes the paper.

## II. COUPLED PLANE WAVES EQUATIONS, POLES, AND ZEROS OF THE FABRY-PÉROT RESONATOR

In this section, we revisit several basic facts about the Fabry-Pérot interferometer and describe its optical properties in terms of the poles and zeros of the reflection coefficient. The introduced notation and the equations obtained here will be used to formulate the spatiotemporal CMT in the subsequent sections.

### A. Scattering matrix of the interfaces and coupled plane waves

We will consider structures with a horizontal symmetry plane, therefore, each interface can be described by the same scattering matrix

$$\mathbf{S} = \begin{bmatrix} r_1 & t_1 \\ t_1 & r_2 \end{bmatrix}, \quad (1)$$

where  $t_1$  is the transmission coefficient,  $r_1$  is the superstrate-to-superstrate reflection coefficient, and  $r_2$  is the reflection coefficient for the plane wave propagating inside the slab.

We will assume that the considered structure contains only lossless materials so that the scattering matrix  $\mathbf{S}$  is unitary:  $\mathbf{S}^\dagger \mathbf{S} = \mathbf{I}$ , where  $\mathbf{I}$  is the identity matrix and dagger denotes Hermitian conjugation. The unitarity, which is a form of writing the energy conservation law, imposes the following relations on the  $S$ -matrix elements:

$$r_1^* = r_2/\Delta, \quad r_2^* = r_1/\Delta, \quad t_1^* = -t_1/\Delta, \quad (2)$$

which directly follow from  $\mathbf{S}^\dagger = \mathbf{S}^{-1} = \text{adj } \mathbf{S}/\Delta$ , where  $\Delta = \det \mathbf{S} = r_1 r_2 - t_1^2$ .

To obtain the complex reflection and transmission coefficients of the Fabry-Pérot resonator, let us represent the field inside and outside the structure as sums of plane waves having the same in-plane wave-vector component

$$k_x = \frac{\omega}{c} n_s \sin \theta,$$

where  $\omega$  is the angular frequency of light,  $n_s$  is the refractive index of the superstrate and substrate, and  $\theta$  is the angle of incidence. The propagation directions of the introduced plane waves are shown in Fig. 1(a). According to this figure, we consider two incident plane waves: the wave in the superstrate with complex amplitude  $I$  and the one in the substrate with complex amplitude  $J$ . The complex amplitudes of the waves inside the structure are denoted as  $U$  and  $D$ . The scattered plane waves with complex amplitudes  $R$  and  $T$  will be referred to as the reflected and transmitted waves, respectively.

Using the scattering matrix (1), we couple the amplitudes of the waves at the slab interfaces, which brings us to the following equations:

$$\begin{aligned} R &= r_1 I + t_1 \xi U, \\ D &= t_1 I + r_2 \xi U, \\ U &= r_2 \xi D + t_1 J, \\ T &= t_1 \xi D + r_1 J, \end{aligned} \quad (3)$$

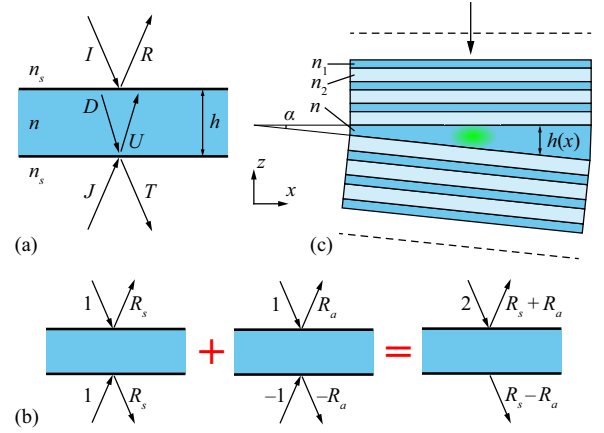


FIG. 1. (a) Fabry-Pérot resonator and the directions of the plane waves constituting the field inside and outside the resonator. (b) One-sided excitation represented as a sum of symmetric and antisymmetric solutions. (c) Linear variable filter based on a wedged phase-shifted Bragg grating simulated using the developed CMT.

where the phase shift acquired by the waves upon propagation between the interfaces is described by the term

$$\xi = \exp \left\{ ih \sqrt{\left( \frac{\omega}{c} n \right)^2 - k_x^2} \right\}, \quad (4)$$

with  $n$  and  $h$  being the refractive index and thickness of the slab, respectively. In Eq. (3),  $I$ ,  $R$ , and  $D$  denote the amplitudes of the waves at the upper interface of the slab, whereas  $J$ ,  $T$ , and  $U$  describe the amplitudes of the waves at the lower interface.

Let us note that we introduced two incident plane waves,  $I$  and  $J$ , to simplify the further analysis. However, at the end, we will be interested in finding the reflected and transmitted field in the case when there is only one incident wave ( $I = 1$  and  $J = 0$ ). In this case, the amplitudes  $R$  and  $T$  become the complex reflection and transmission coefficients of the Fabry-Pérot resonator and can be obtained from Eqs. (3) in the following well-known form:

$$R = r_1 + r_2 \frac{t_1^2 \xi^2}{1 - r_2^2 \xi^2}, \quad T = \frac{t_1^2 \xi}{1 - r_2^2 \xi^2}. \quad (5)$$

### B. Zeros of the reflection coefficient

Let us analyze the expression (5) for the reflection coefficient in the case of normal incidence of light (i.e., at  $k_x = 0$ ). In particular, let us find such a frequency  $\omega_0$  that the reflection vanishes:  $R(\omega_0, k_x = 0) = 0$ . Solving this equation gives  $\zeta^2 = r_1/(r_2 \Delta)$ , where  $\zeta$  denotes  $\xi$  evaluated at  $\omega = \omega_0$  and  $k_x = 0$ :

$$\zeta = \exp \left\{ ih \frac{\omega_0}{c} n \right\}. \quad (6)$$

The unitarity consequences (2) allow one to rewrite the condition for the reflection coefficient to be zero as

$$\zeta^2 = \frac{r_2^*}{r_2}. \quad (7)$$

Note that the right-hand side of this equation has unit modulus, therefore, Eq. (7) can be satisfied at  $k_x = 0$  and at a *real* frequency

$$\omega_0 = \frac{c}{nh}(\pi k - \arg r_2), \quad k \in \mathbb{Z}. \quad (8)$$

At this frequency, the considered Fabry-Pérot resonator works as a spectral filter in the case of normal incidence of light. It is this frequency, in the vicinity of which we will construct an approximation leading to the CMT.

For further derivations, let us note that

$$r_2 \zeta = |r_2| e^{i \arg r_2} \times e^{i \pi k} e^{-i \arg r_2} = (-1)^k |r_2|, \quad (9)$$

which is a real number.

Let us now show that the zeros defined by the even (odd) values of  $k$  arise due to the excitation of symmetric (antisymmetric) eigenmodes of the structure. To do this, in the following two subsections we find the eigenfrequencies of the symmetric and antisymmetric modes of the Fabry-Pérot interferometer, which are excited at  $k_x = 0$ . Let us note that the eigenmodes studied in this work are the leaky ones possessing complex frequencies.

### C. Poles in the case of a symmetric excitation

We first consider the case of symmetric excitation, that is,  $I = J$ . In this case, the scattered field and the field inside the structure are also symmetric, which gives  $R = T$  and  $D = U$ , respectively. The coupled plane waves Eqs. (3) take the following simple form:

$$\begin{aligned} R_s &= r_1 I + t_1 \xi U, \\ U &= r_2 \xi U + t_1 I, \end{aligned} \quad (10)$$

where we denote the ‘‘symmetric’’ reflected wave amplitude  $R$  by  $R_s$ .

To find the symmetric eigenmodes, we express  $R_s$  from Eq. (10) at  $I = 1$ , which gives

$$R_s = \frac{\Delta \xi - r_1}{r_2 \xi - 1} \quad (11)$$

and find such a complex  $\omega$  that the denominator in  $R_s$  vanishes. This happens when  $\xi = r_2^{-1}$ , i.e., at  $\omega = \omega_{p,2l}$ , where

$$\omega_{p,2l} = \frac{c}{nh}(2\pi l - \arg r_2 + i \ln|r_2|), \quad l \in \mathbb{Z}. \quad (12)$$

Here, we assume  $k_x = 0$ , therefore, we obtain eigenfrequencies of the modes excited by a normally incident plane wave. Since we assume the incident field to be symmetric, the obtained eigenmode is a  $z$ -symmetric one, which scatters symmetrically to the substrate and superstrate.

### D. Poles in the case of an antisymmetric excitation

The case of antisymmetric excitation ( $J = -I$ , hence  $T = -R$  and  $D = -U$ ) is considered similarly to the previous subsection. The coupled plane waves equations take the following form:

$$\begin{aligned} R_a &= r_1 I + t_1 \xi U, \\ -U &= r_2 \xi U + t_1 I, \end{aligned} \quad (13)$$

where we introduce  $R_a$  denoting the reflected field amplitude  $R$  in the case of an antisymmetric excitation. The antisymmetric eigenmodes are calculated as the poles of

$$R_a = \frac{\Delta \xi + r_1}{r_2 \xi + 1}. \quad (14)$$

The poles are found by equating the denominator in  $R_a$  to zero, which yields  $\xi = -r_2^{-1}$ . Therefore, assuming  $k_x = 0$ , we can write down the complex frequencies of the eigenmodes as

$$\omega_{p,2l+1} = \frac{c}{nh}[(2l+1)\pi - \arg r_2 + i \ln|r_2|], \quad l \in \mathbb{Z}. \quad (15)$$

These are the frequencies of the  $z$ -antisymmetric eigenmodes, which scatter to the substrate and superstrate out of phase.

From Eqs. (8), (12), and (15), we can conclude that the real parts of the complex eigenfrequencies match the reflection zeros. From these equations, it follows that the reflection zeros calculated using Eq. (8) at even  $k$  values are associated with the excitation of symmetric eigenmodes, whereas the odd values of  $k$  correspond to antisymmetric modes. We will use this important fact in the following derivations.

### E. Numerical example

Let us consider an example of the Fabry-Pérot interferometer, in which the reflection and transmission coefficients are assumed to be constant:  $t_1 = 0.6$ ,  $r_2 = -r_1 = 0.8$ ; the corresponding scattering matrix is, obviously, unitary. We consider a slab with the thickness  $h = 1 \mu\text{m}$  and refractive index  $n = 2$ . The results based on Eq. (5) are presented in Fig. 2(a). The calculations were performed above the light lines. One can see three pronounced resonant curves in the figure with the middle one corresponding to a symmetric mode [with  $2l = 2$  in Eq. (12)] and the other two emerging due to the excitation of antisymmetric eigenmodes [with  $2l + 1 = 1, 3$  in Eq. (15)]. In the following two sections, we will use this example to illustrate how the developed CMT describes the optical properties of the Fabry-Pérot interferometer.

## III. COUPLED-MODE THEORY BASED ON $\omega$ -SYMMETRIC APPROXIMATION

In this section, we derive a spatiotemporal coupled-mode theory for the Fabry-Pérot resonator. To do this, we make an important assumption that the elements of the scattering matrix (1) are constant and, thus, do not depend on  $\omega$  or  $k_x$ . In this case, the only  $\omega$ - and  $k_x$ -dependent quantity is  $\xi$  in Eq. (4). To obtain the CMT, we will be replacing  $\xi(\omega, k_x)$  with an algebraic expression that approximates it in a vicinity of the point  $k_x = 0$ ,  $\omega = \omega_0$ . Importantly, the form of such an approximation should preserve the symmetry properties of the considered diffraction problem.

### A. Unitary approximation for $\xi$

Let us start with a simple Taylor approximation for  $\xi(\omega, k_x)$  defined in Eq. (4). However, instead of directly expanding this function, we consider  $\xi$  as function of  $k_x$  and  $q = \omega^2$ , which we denote as  $\eta(q, k_x) = \exp\{ih\sqrt{qn^2c^{-2} - k_x^2}\}$ . By writing the Taylor series for this function about the point

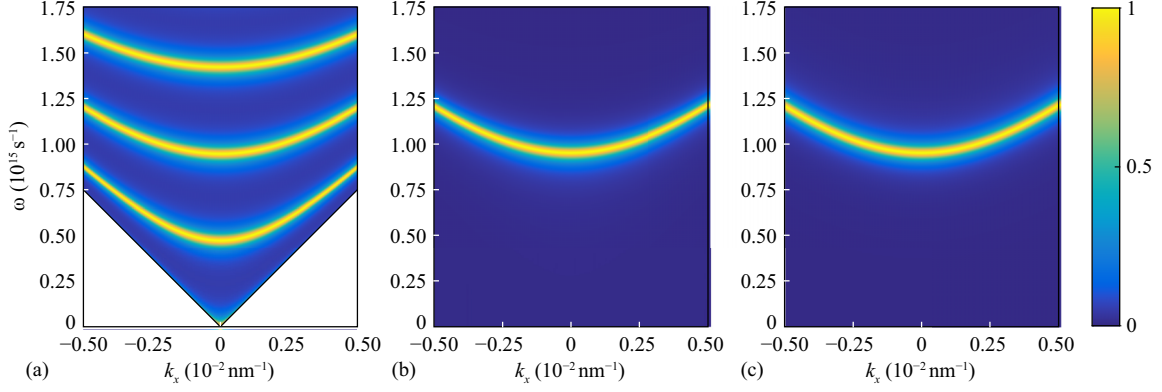


FIG. 2. Intensity of light transmitted through the Fabry-Pérot resonator at different angular frequencies  $\omega$  and different values of the in-plane wave-vector component  $k_x$ . Intensity was calculated using (a) exact Eq. (5), (b) approximate Eq. (32) based on  $\omega$ -symmetric CMT, and (c) approximate Eq. (37) based on causal CMT.

$q = \omega_0^2$ ,  $k_x = 0$ , we obtain

$$\xi(\omega, k_x) = \eta(\omega^2, k_x) \approx \zeta \left[ 1 - i \frac{hc}{2n\omega_0} k_x^2 + i \frac{nh}{c} \frac{\omega^2 - \omega_0^2}{2\omega_0} \right], \quad (16)$$

where  $\zeta$  is defined in Eq. (6).

Note that the quantity  $\xi$  does not have unit modulus, whereas its Taylor approximation (16) no longer does. Using such an approximation would result in the violation of the energy conservation law. To overcome this problem, let us consider another approximation for  $\xi$  preserving the unit modulus. Since  $|\xi| = |\sqrt{\xi}| = 1$ , the complex conjugate of  $\sqrt{\xi}$  is  $(\sqrt{\xi})^* = 1/\sqrt{\xi}$ . This allows us to write  $\xi = \sqrt{\xi}/(\sqrt{\xi})^*$ , and by replacing  $\sqrt{\xi}$  in this expression with its Taylor expansion similar to Eq. (16), we arrive at the approximation we will be using in this section:

$$\xi(\omega, k_x) \approx -\zeta \frac{v_g^2 k_x^2 - (\omega^2 - \omega_0^2) + \frac{4ic}{nh} \omega_0}{v_g^2 k_x^2 - (\omega^2 - \omega_0^2) - \frac{4ic}{nh} \omega_0}. \quad (17)$$

Here,  $v_g = c/n$  is the phase velocity of light in the slab. Note that the numerator in this approximation is the complex conjugate of the denominator, which ensures that the energy conservation law is not violated. It should also be noted that the obtained approximation is an even function of the angular frequency  $\omega$ ; therefore, we refer to this approximation as  $\omega$ -symmetric.

To obtain a form of the CMT that takes into account the presence of the horizontal symmetry plane in the structure, below we apply the obtained approximation (17) separately for the cases of  $z$ -symmetric ( $I = J$ ) and  $z$ -antisymmetric ( $I = -J$ ) excitations.

### B. CMT for a symmetric excitation

In this subsection, we will develop the coupled-mode theory for the case of symmetric excitation. Therefore, we will work with the corresponding symmetric coupled plane waves model of Eq. (10) from Sec. II C. To obtain an equation in the form of coupled-mode theory [12], we have to perform the following change of variables: instead of the unknown amplitude  $U$ , we will use the quantity  $W = t_1 \xi U + \alpha I$ , where

$\alpha$  is a constant defined below. The physical meaning of  $W$  will be discussed below [after Eq. (27)]. By rewriting Eq. (10) in terms of  $W$ , we obtain

$$W - \alpha I = r_2 \xi (W - \alpha I) + \xi t_1^2 I, \quad (18)$$

$$R_s = (r_1 - \alpha)I + W. \quad (19)$$

Then, we apply the approximation (17), which leads us to a quite complicated expression (not presented here for the sake of brevity) containing  $W$ ,  $\omega^2 W$ ,  $k_x^2 W$ ,  $I$ ,  $\omega^2 I$ , and  $k_x^2 I$  terms. However, if we assume  $\alpha = t_1^2 \zeta / (r_2 \zeta + 1)$ , we zero out the  $\omega^2 I$  and  $k_x^2 I$  terms and Eq. (18) becomes

$$-\omega^2 W = -v_g^2 k_x^2 W - \omega_0^2 W + \frac{4ic}{nh} \times \frac{1 - r_2 \zeta}{1 + r_2 \zeta} \omega_0 W - \frac{8ic}{nh} \times \frac{t_1^2 \zeta}{(1 + r_2 \zeta)^2} \omega_0 I. \quad (20)$$

Now, let us recall that the frequency  $\omega_0$ , at which the approximation was constructed, is not an arbitrary frequency, but the one defined by Eq. (8). Since in this subsection, we consider the symmetric excitation case, we will assume that the frequency  $\omega_0$  is located near a symmetric mode, i.e.,  $k$  in Eq. (9) is even and  $r_2 \zeta = |r_2|$ . This, along with Eqs. (2), allows us to simplify Eq. (20) and the expression for the reflection coefficient  $R_s$  [Eq. (19)]:

$$-\omega^2 W = -v_g^2 k_x^2 W - \omega_0^2 W + i\gamma \omega_0 W + 2ie^{i\phi} \gamma \omega_0 I, \quad (21)$$

$$R_s = e^{i\phi} I + W, \quad (22)$$

where  $\phi = \arg r_1$  and

$$\gamma = \frac{4c}{nh} \times \frac{1 - |r_2|}{1 + |r_2|}. \quad (23)$$

Solving Eqs. (21) and (22) for  $R_s$  at  $I = 1$  gives the complex reflection coefficient for the case of symmetric excitation

$$R_s(\omega, k_x) = e^{i\phi} + e^{i\phi} \frac{2i\omega_0 \gamma}{v_g^2 k_x^2 - \omega^2 + \omega_0^2 - i\omega_0 \gamma}. \quad (24)$$

Here, the first term  $R_{s, \text{nr}} = e^{i\phi}$  is the background (nonresonant) reflection coefficient (i.e., the value of the reflection

coefficient at  $\omega$  far from the resonance). The second term in Eq. (24) describes resonant scattering of light. In this regard, Eq. (24) is similar to the equation describing the Fano resonance [3,27], in which the resonant and nonresonant scattering processes are written separately. Bringing the nonresonant and resonant terms to a common denominator makes it obvious that  $|R_s| = 1$ .

Let us now obtain the CMT. To do this, we apply the Fourier transform  $\mathcal{F}$  [13] defined as

$$[\mathcal{F}G](t, x) = \iint_{\mathbb{R}^2} G(\omega, k_x) e^{ik_x x - i\omega t} dk_x d\omega \quad (25)$$

to the left- and right-hand sides of Eqs. (21) and (22):

$$\frac{\partial^2 w}{\partial t^2} = v_g^2 \frac{\partial^2 w}{\partial x^2} - \omega_0^2 w + i\gamma \omega_0 w + 2ie^{i\phi} \gamma \omega_0 f_I(t, x), \quad (26)$$

$$f_{R,s}(t, x) = e^{i\phi} f_I(t, x) + w(t, x). \quad (27)$$

Here, the Fourier images are the spatiotemporal field distributions of the scattered field ( $f_{R,s} = \mathcal{F}R_s$ ), of the mode ( $w = \mathcal{F}W$ ), and of the incident field ( $f_I = \mathcal{F}I$ ). The obtained Eqs. (26) and (27) relate these fields and, therefore, can be considered as a coupled-mode theory describing the considered diffraction problem. In this regard, the quantity  $W$  introduced in this section is the spectrum of the excited eigenmode of the structure.

It is noteworthy that the obtained PDE (26) can be considered as a nonuniform wave equation. Indeed, the part  $\frac{\partial^2 w}{\partial t^2} = v_g^2 \frac{\partial^2 w}{\partial x^2} - \omega_0^2 w$  is the wave equation for a medium with a hyperbolic dispersion law  $\omega^2 = v_g^2 k_x^2 + \omega_0^2$ . The  $i\gamma \omega_0 w$  term in Eq. (26) describes the leakage of the eigenmode and the last term  $2ie^{i\phi} \gamma \omega_0 f_I$  describes the excitation of the eigenmode by the incident field.

If we now consider a monochromatic field with the time dependence of  $e^{-i\omega t}$ , Eq. (26) will become a spatial formulation of the CMT [1]. Similarly, by considering fields depending on the spatial variable  $x$  as  $e^{ik_x x}$ , we will get a second-order differential equation, which can be transformed using the slowly varying envelope approximation to obtain the temporal coupled-mode theory [3]. In this regard, the obtained PDE describing both temporal and spatial evolution of the field will be referred to as the spatiotemporal coupled-mode theory.

### C. CMT for an antisymmetric excitation

Deriving the CMT for the antisymmetric excitation is very much similar to the symmetric case. We start from Eq. (13), introduce a new unknown  $W = t_1 \xi U + \alpha I$  with  $\alpha = t_1^2 \zeta / (r_2 \zeta - 1)$ , and apply the approximation (17). Then, we assume that the frequency  $\omega_0$  is located near an antisymmetric mode, i.e.,  $k$  in Eq. (6) is odd and  $r_2 \zeta = -|r_2|$ . This brings us to

$$R_a = e^{i\phi} I + W, \quad (28)$$

where  $W$  turns out to satisfy the very same relation (21) as in the symmetric case. Despite the fact that this equation has the same form for the symmetric and antisymmetric cases, the  $\omega_0$  values in these two cases are different. Indeed, the value of  $\omega_0$  is calculated using Eq. (8) with  $k$  being even in the symmetric case, whereas the odd values of  $k$  have to be used when describing the antisymmetric excitation. Keeping that

in mind, we can use the CMT equation (26), which enables expressing the reflected signal as

$$f_{R,a}(t, x) = e^{i\phi} f_I(t, x) + w(t, x), \quad (29)$$

where  $f_{R,a} = \mathcal{F}R_a$ . Obviously, the reflection coefficient also takes the same form as  $R_s$ :

$$R_a(\omega, k_x) = e^{i\phi} + e^{i\phi} \frac{2i\omega_0 \gamma}{v_g^2 k_x^2 - \omega^2 + \omega_0^2 - i\omega_0 \gamma}. \quad (30)$$

### D. CMT for a one-sided excitation

Let us now obtain approximate expressions for the reflection and transmission coefficients in the case of one-sided excitation of the structure by a plane wave incident from the superstrate, i.e., when  $I = 1, J = 0$ . To do this, we represent such a solution as half the sum of a symmetric solution with  $I = J = 1$  and an antisymmetric solution with  $I = -J = 1$  [see Fig. 1(b)]:

$$R = \frac{R_s + R_a}{2}, \quad T = \frac{R_s - R_a}{2}, \quad (31)$$

where  $R_s$  is given by Eq. (24) and  $R_a$  is defined in Eq. (30).

Before moving further, we should recall that the two referenced equations were obtained to describe different eigenmodes: Eq. (24) describes reflection of light when a symmetric mode is excited, whereas Eq. (30) corresponds to the excitation of an antisymmetric mode. Let us consider these two cases separately. If we want to describe the optical properties of the Fabry-Pérot resonator near a frequency of a symmetric mode ( $k$  is even), we should use Eq. (24) for the  $R_s$  term in Eq. (31), yet in the  $R_a$  term [see Eq. (30)], we can neglect the resonant part assuming that the antisymmetric mode is not excited when we are near the frequency of a symmetric mode. Therefore, we assume that  $R_a$  is equal to  $R_{nr} = e^{i\phi}$  and obtain

$$R = \frac{R_s + R_{nr}}{2}, \quad T = \frac{R_s - R_{nr}}{2}.$$

Similarly, to describe the excitation of an antisymmetric mode ( $k$  is odd), we keep the resonant term in Eq. (30) and neglect the excitation of the neighboring symmetric modes:

$$R = \frac{R_{nr} + R_a}{2}, \quad T = \frac{R_{nr} - R_a}{2}.$$

The general expressions for the reflection and transmission coefficients, which are valid for both considered cases, are

$$R(\omega, k_x) = e^{i\phi} \frac{v_g^2 k_x^2 - \omega^2 + \omega_0^2}{v_g^2 k_x^2 - \omega^2 + \omega_0^2 - i\omega_0 \gamma}, \quad (32)$$

$$T(\omega, k_x) = (-1)^k e^{i\phi} \frac{i\omega_0 \gamma}{v_g^2 k_x^2 - \omega^2 + \omega_0^2 - i\omega_0 \gamma}.$$

One can easily show that the CMT in the case of one-sided excitation is still described by Eq. (26) and by

$$f_R(t, x) = e^{i\phi} f_I(t, x) + \frac{w(t, x)}{2}, \quad f_T(t, x) = (-1)^k \frac{w(t, x)}{2}, \quad (33)$$

where  $f_R = \mathcal{F}R$  and  $f_T = \mathcal{F}T$  are the field distributions of the reflected and transmitted light.

Let us note that layered structures like the ones considered in this work can be analyzed using the spatial formulation of the CMT [5–7,28]. Comparing to the spatial CMT, the proposed spatiotemporal CMT formulation contains the second-order spatial derivative, which makes it suitable for describing the optical properties of layered structures in the vicinity of normal incidence. In addition, the presence of temporal derivative in the CMT allows one to take into account the frequency (wavelength) in the model. In particular, Eq. (32) providing explicit dependence on both  $\omega$  and  $k_x$  makes the spatiotemporal CMT a powerful tool for describing spatiotemporal pulse transformation by layered resonant structures [29].

### E. Numerical example

Let us demonstrate that the derived Eq. (32) describes the resonant curves in Fig. 2(a) in the  $\omega$ - $k_x$  parameter space. To use Eq. (32), we have to choose a particular value of  $k$  in Eq. (8); by doing this, we can make the CMT model to describe one of the resonant curves in Fig. 2(a). As an example, we chose the middle one corresponding to  $k = 2$  so that the approximation was carried out in the vicinity of  $\omega_0 = 0.9418 \times 10^{15} \text{ s}^{-1}$ . The approximated  $\omega$ - $k_x$  transmittance spectrum calculated using Eq. (32) is shown in Fig. 2(b). It is evident that the line shape, width, and the dispersion of the resonant curve on the CMT plot is in good agreement with the corresponding resonant curve in Fig. 2(a). Indeed, the root-mean-square error between the exact and approximated *complex* amplitudes calculated in the region  $\omega \in [0.75, 1.25] \times 10^{15} \text{ s}^{-1}$ ,  $|k_x| < 2.5 \times 10^{-3} \text{ nm}^{-1}$  amounts to only  $3.4 \times 10^{-3}$ .

## IV. CAUSAL CMT BASED ON AN HERMITIAN APPROXIMATION

Let us note that the CMT formulation obtained in the previous section has a notable drawback. According to Eq. (32), at a fixed value of  $k_x$ , its denominator diverges at two distinct complex frequencies. The first one has a positive real part and a negative imaginary part. This is the “physical” eigenmode, which we investigate. The second one has a negative real part and a positive imaginary part. The fact that the imaginary part of the complex frequency of the second mode is negative violates the causality condition. While this has no implications when describing the reflection and transmission spectra, the violation of causality is undesirable when investigating spatiotemporal pulse transformations [30] since it leads to a nonphysical form of the pulse response of the structure. In this regard, for certain applications, another approximation, which we derive in this section, might be more favorable.

### A. Hermitian symmetry and causality

Let us require the approximating reflection (and transmission) coefficient to be an Hermitian function, i.e., we require its values at negative and positive frequencies to be related as [31,32]

$$R(-\omega) = R^*(\omega), \quad \omega \in \mathbb{R}.$$

Such symmetry, as we demonstrate in this section, provides the functions  $R(\omega)$  and  $T(\omega)$  to be holomorphic in the

upper half of the complex frequency plane, which ensures the causality condition.

To obtain such approximations, we will construct an Hermitian unitary approximation for  $\xi$  defined in Eq. (4) instead of using the  $\omega$ -symmetric unitary approximation of Eq. (17). Besides, in order for the resulting approximations for  $R$  and  $T$  to be Hermitian as well, we have to assume that the local reflection and transmission coefficients ( $r_1, r_2, t_1$ ) of the interfaces of the considered structure also satisfy this requirement. Since these quantities are assumed constant, the hermiticity property requires  $r_1, r_2, t_1$  to be real numbers. This is exactly the case for several practically important structures, e.g., dielectric Fabry-Pérot resonators (including the ones with Bragg claddings), for which the scattering matrix  $\mathbf{S}$  describing the claddings indeed contains only real numbers in the case of normal incidence of light. Assuming  $r_2$  being real allows us to rewrite Eq. (8) in the following simple form:

$$\omega_0 = \frac{c}{nh} \pi(k - m), \quad k \in \mathbb{Z}, \quad (34)$$

where  $m = 0$  when  $r_2$  is positive and  $m = 1$  otherwise [i.e.,  $r_2 = (-1)^m |r_2|$ ]. In this case, Eq. (6) yields  $\zeta = (-1)^{k-m}$ .

### B. Hermitian unitary approximation for $\xi$

Before constructing an Hermitian approximation for  $\xi$  defined in Eq. (4), let us note that the quantity  $\xi$  contains a square root, which is a two-valued function. Having chosen the value of the square root at the positive frequency  $\omega_0$  from the physical meaning of the problem being solved, we still have two options in choosing the value at the negative frequency  $-\omega_0$ . In Sec. III, we considered one such option requiring  $\xi(-\omega) = \xi(\omega)$  for the approximating expression. In this section, we will require  $\xi(-\omega) = [\xi(\omega)]^*$ , i.e., we require  $\xi$  to be an Hermitian function. Let us note that these two cases correspond to different trajectories on the complex plane when constructing the analytical continuation from the point  $\omega_0$  to the point  $-\omega_0$ .

Requiring the approximation of  $\xi$  to be Hermitian and unitary leads to the following approximation, which is derived in Appendix A:

$$\xi(\omega, k_x) \approx (-1)^{k-m+1} \frac{v_g^2 k_x^2 - (\omega^2 - \omega_0^2) + \frac{4ic}{nh} \omega}{v_g^2 k_x^2 - (\omega^2 - \omega_0^2) - \frac{4ic}{nh} \omega}. \quad (35)$$

Comparing this approximation with Eq. (17) obtained in the  $\omega$ -symmetric case, two differences have to be noted. The first one is the explicit form of the coefficient before the fraction, which follows from Eq. (34). The main difference is that the last terms in both the numerator and denominator contain  $\omega$  instead of  $\omega_0$ . Nevertheless, the similarities between Eqs. (17) and (35) make the derivation of the CMT almost identical to the one presented in the previous section.

### C. Coupled-mode theory

Following the same steps as in Secs. III B to III D brings us to a new form of the coupled-mode equation

$$\frac{\partial^2 w}{\partial t^2} + \gamma \frac{\partial w}{\partial t} = v_g^2 \frac{\partial^2 w}{\partial x^2} - \omega_0^2 w - 2e^{i\phi} \gamma \frac{\partial f_I}{\partial t}, \quad (36)$$

which is a nonuniform damped wave equation with an additional term  $\omega_0^2 w$  describing the dispersion of the considered eigenmode. Note that it is the derivative of the incident signal, which makes this equation nonuniform, and not the signal itself as in Eq. (26). The reflected and transmitted fields can still be calculated using Eq. (33). The corresponding approximations for the reflection and transmission coefficients have the following form:

$$R(\omega, k_x) = e^{i\phi} \frac{v_g^2 k_x^2 - \omega^2 + \omega_0^2}{v_g^2 k_x^2 - \omega^2 + \omega_0^2 - i\omega\gamma}, \quad (37)$$

$$T(\omega, k_x) = (-1)^k e^{i\phi} \frac{i\omega\gamma}{v_g^2 k_x^2 - \omega^2 + \omega_0^2 - i\omega\gamma},$$

where  $e^{i\phi} = \text{sgn } r_1 = (-1)^{m+1}$ .

Comparing the last equation with the results of Sec. III, we can infer that the only difference is the  $i\omega\gamma$  term, which appears instead of  $i\omega_0\gamma$  [cf. Eq. (32)]. This seemingly little difference has an important consequence that in the obtained approximations (37), the eigenfrequencies always have negative imaginary parts, which allows us to refer to such an approximation as causal. Indeed, one can show that for such approximations, the impulse response is nonzero only inside the light cone [30,33]. This makes the Hermitian approximation useful when describing spatiotemporal shaping of optical pulses by resonant structures (see, e.g., [29,30]). However, the  $\omega$ -symmetric approximation of Sec. III, which is simpler, might be more convenient for theoretical analysis of monochromatic light diffraction and description of structures, for which the scattering matrix  $\mathbf{S}$  might contain complex numbers.

#### D. Numerical example

Figure 2(c) shows the transmittance spectrum calculated using Eq. (37) at  $k = 2$ . The root-mean-square deviation of the approximated complex amplitude from the exact one [Fig. 2(a)] calculated in the region  $\omega \in [0.75, 1.25] \times 10^{15} \text{ s}^{-1}$ ,  $|k_x| < 2.5 \times 10^{-3} \text{ nm}^{-1}$  amounts to  $2.6 \times 10^{-3}$ , therefore, as in the previous case, the derived causal CMT provides a good approximation for the resonant curve.

For a more detailed comparison between the two derived CMT models, we considered the vertical cross sections of the plots from Fig. 2. These cross sections calculated at  $k_x = 0$  are shown in Fig. 3, according to which, the  $\omega$ -symmetric approximation of Sec. III D provides a slightly better agreement at the frequencies below  $\omega_0$ , whereas the Hermitian approximation from Sec. IV C gives better results at  $\omega > \omega_0$ . In this regard, one should rely on other reasons rather than the accuracy when choosing between the two presented approximations, as we discussed in the end of the previous subsection.

### V. APPLICATION TO A LINEAR VARIABLE FILTER BASED ON A PHASE-SHIFTED BRAGG GRATING

#### A. Geometry of the structure

Let us now consider a more sophisticated example demonstrating the applicability range of the developed CMT, namely, a Fizeau interferometer, which is a wedged version of the

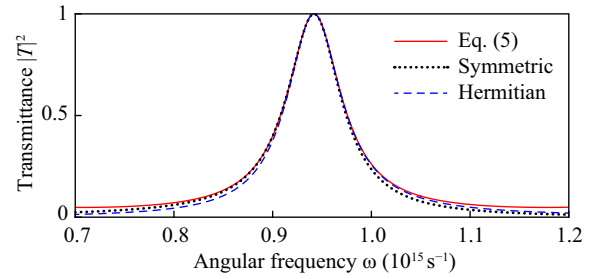


FIG. 3. Intensity of light transmitted through the Fabry-Pérot resonator at different angular frequencies  $\omega$  in the case of normal incidence calculated using Eq. (5) (solid red line),  $\omega$ -symmetric approximation of Eq. (32) (dotted black line), and Hermitian approximation of Eq. (37) (dashed blue line).

Fabry-Pérot interferometer. As a particular structure, we will consider a phase-shifted Bragg grating (PSBG) with a wedge-shaped central layer as shown in Fig. 1(c). Such structures, nowadays referred to as linear variable filters (LVF), are widely used in modern microspectrometers [16,18], sensors [22], and hyperspectral imaging systems [25].

Each Bragg mirror of the considered structure consists of three pairs of layers with refractive indices  $n_1 = 2.1$  and  $n_2 = 1.45$ , which correspond to  $\text{TiO}_2$  and  $\text{SiO}_2$ , respectively. The thicknesses of the layers were calculated from the Bragg condition  $h_i = \lambda_B / (4n_i)$ ,  $i = 1, 2$ , where  $\lambda_B = 800 \text{ nm}$ . The central layer has a refractive index  $n = n_2 = 1.45$  and a linearly varying thickness

$$h(x) = h_0 + x \tan \alpha, \quad (38)$$

where  $\alpha = 0.5^\circ$  is the wedge angle and  $h_0 = \lambda_B / (2n) = 190 \text{ nm}$  is the thickness of the central layer at  $x = 0$ . Therefore, the mode excitation condition at  $x = 0$  is fulfilled for normally incident light having the wavelength  $\lambda_B = 800 \text{ nm}$ .

We will assume that a monochromatic plane wave is normally incident on the considered structure. Depending on the wavelength of the incident light, the Fabry-Pérot resonance condition (8) will take place at different points along the structure. Therefore, we expect the light with different wavelengths to be transmitted at different spatial positions  $x$ . Such an optical property of LVFs is beneficial for spectrometric and hyperspectral applications [16,18,25].

#### B. Local uniform approximation and rigorous numerical simulations

When the wedge angle  $\alpha$  is very small, we can calculate the local reflectance and transmittance by simply substituting Eq. (38) into Eq. (5). This means that we replace the structure with a uniform nonwedged structure having the central layer thickness  $h$  equal to the *local* thickness  $h(x)$  of the considered structure. We will refer to this approach as the *local uniform approximation*. The transmittance and reflectance plots calculated using this approach are shown in Fig. 4 with dashed blue lines. We can see a pronounced Lorentzian peak in the transmittance and a corresponding dip in the reflectance plot.

The local uniform approximation is valid when the wedge angle  $\alpha$  is very small. However, even for values of  $\alpha$  as small as the considered value  $0.5^\circ$ , a more accurate treat-

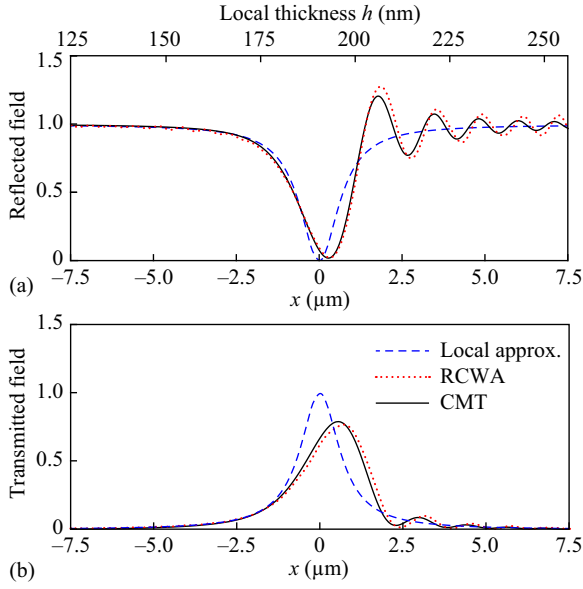


FIG. 4. (a) Reflected and (b) transmitted field distributions of the LVF calculated using the local uniform approximation (dashed blue lines), RCWA (dotted red lines), and the developed CMT (solid black lines).

ment is required. To demonstrate this, we utilize the RCWA, an established numerical tool for solving Maxwell's equations [26,34]. Since RCWA is aimed at simulating periodic structures, we considered a 15- $\mu\text{m}$  part of the wedged PSBG covering  $x \in [-7.5, 7.5] \mu\text{m}$ . Then, we periodized this part along the  $x$  axis and optically isolated the adjacent periods with anisotropic PML layers. The upper Bragg grating interface was aligned with the  $x$  axis, whereas the tilted lower Bragg grating was replaced with its staircase approximation consisting of 500 layers. The simulations were performed using  $2 \times 100 + 1$  Fourier harmonics, which turned out to be sufficient for the RCWA to converge. Transverse-electric (TE) polarization of the incident wave was considered in the simulations. To compare the RCWA results with the CMT, we calculate the reflected and transmitted field distributions  $|E_y|^2$  along the dashed lines shown in Fig. 1(c). These lines are 250 nm above and below the structure; such distance is required to exclude evanescent waves from the consideration.

The RCWA simulation results are shown in Fig. 4 with a dotted red line. By comparing the RCWA results with the local uniform approximation, one can see that the rigorous simulations predict a bit broader peak and several secondary peaks appearing to the right of the first one. Such secondary fringes are known to appear in Fizeau interferometers [16,35–37]. Note that both the width of the main peak and the magnitude of the secondary peaks depend on the wedge angle. If we decrease the wedge angle, the secondary fringes in the RCWA spectrum will disappear and the line shape will converge to the Lorentzian one predicted by the local uniform approximation. However, witnessing such a convergence is hardly possible using RCWA since rigorous simulations are rather time and memory consuming. For the considered case, the simulations take about 8 minutes, yet for smaller wedge angles, which are more interesting for practical applications due to smaller secondary fringes, the required time grows rapidly. In this regard,

a faster approach for simulating PSBGs with nonconstant (and not necessarily linearly varying) central layer thickness is desirable. Below, we show that the developed CMT can be considered as such an approach.

### C. Application of the coupled-mode theory

To describe the considered wedged structure with the developed CMT, we rely on Eq. (26), which was obtained within the  $\omega$ -symmetric approximation. Since in this structure, the thickness of the central layer varies along the  $x$  direction, the parameters of the CMT  $\omega_0$ ,  $\gamma$ , and  $v_g$  will no longer be constant.

Obviously, the frequency of the reflection zero  $\omega_0$  in Eq. (26) depends on the layer thickness  $h$ , therefore,  $\omega_0$  will become  $x$  dependent when describing a wedged structure. Moreover, in the considered example, the dependence of the reflection coefficient  $r_2$  on  $\omega$  also becomes important. In this regard, the frequency  $\omega_0$  should be determined as the solution of the following equation:

$$\omega_0(x) = \frac{c}{nh(x)} \{\pi k - \arg r_2[\omega_0(x)]\}. \quad (39)$$

Regarding the parameters  $\gamma$  and  $v_g$ , the simulations (not presented here for the sake of brevity) show that taking into account their dependence on  $x$  leads to only marginal changes in the resulting reflected and transmitted fields. In this regard, in the following simulations, we will assume that  $\gamma$  and  $v_g$  are constant. However, as we discuss in Appendix B, the dependence of  $r_2$  on  $\omega$  requires us to use not Eq. (23) but more accurate Eq. (B2) for calculating  $\gamma$ . Similarly, the group velocity  $v_g$  has to be calculated using Eq. (B3), which takes into account the dependence of  $r_2$  on both  $\omega$  and  $k_x$ . In the simulations, we used the values  $\gamma = 5.322 \times 10^{13} \text{ s}^{-1}$  and  $v_g = 0.569 c$ , which were calculated in this way at  $h = h_0$ .

Having calculated the parameters of the CMT, we can write down the final form of the differential equation. Since we consider a monochromatic normally incident plane wave with unit amplitude, we assume  $f_i(t, x) = e^{-i\omega t}$ . Therefore, the PDE (26) becomes an ordinary differential equation

$$v_g^2 w''(x) = [\omega_0(x)^2 - \omega^2 - i\gamma\omega_0(x)]w(x) - 2ie^{i\phi}\gamma\omega_0(x). \quad (40)$$

Following the reasoning from Sec. III D, we can calculate the reflected and transmitted field distributions as

$$f_R(x) = e^{i\phi} + \frac{w(x)}{2}, \quad f_T(x) = (-1)^k \frac{w(x)}{2}.$$

Here and in Eq. (40), we omit the  $e^{-i\omega t}$  term, i.e., we use  $w(t, x) = w(x)e^{-i\omega t}$  and similar relations for  $f_R$  and  $f_T$ . To solve the differential equation (40) numerically, we use the shooting method with the boundary conditions  $w(-X) = w(X) = 0$ , where  $X = 7.5 \mu\text{m}$  defines the solution region:  $x \in [-X, X]$ .

The obtained numerical solution is shown in Fig. 4 with solid black lines. For each wavelength, less than 9 seconds were required to solve the CMT equation. It is evident from the figure that the CMT predictions are in good agreement with the RCWA simulation results. The slight difference is mainly due to two facts with the first one being that the



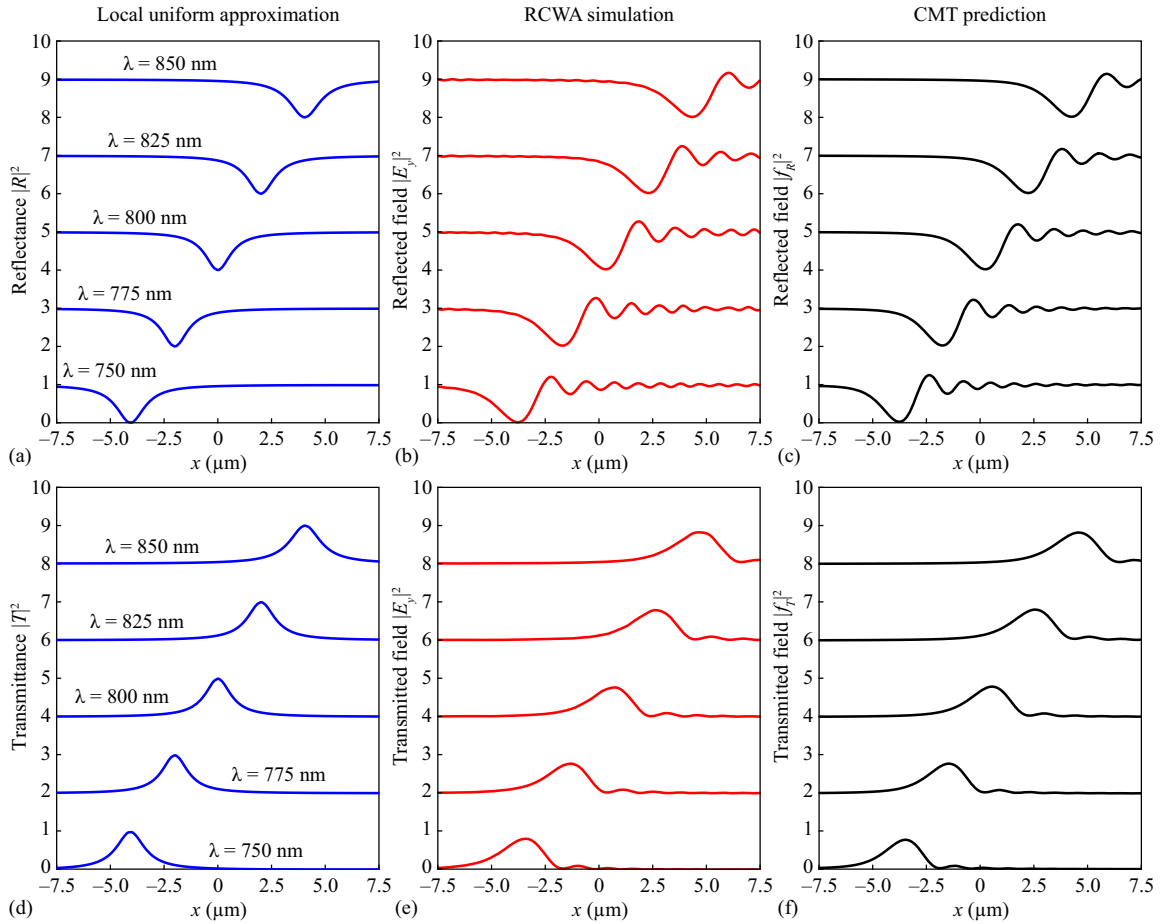


FIG. 5. (a)–(c) Reflected and (d)–(f) transmitted field distributions of the LVF calculated using the (a), (d) local uniform approximation, (b), (e) RCWA, and (c), (f) the developed CMT. The plots calculated at different wavelengths are vertically shifted by two units each for visual clarity.

constant values of  $v_g$  and  $\gamma$  were considered in the CMT. The second one is that in the RCWA, the reflected and transmitted field distributions were calculated not on the PSBG interfaces but along the dashed lines [see Fig. 1(c)], therefore, the shapes of the reflected and transmitted beams were slightly changed due to propagation. Note that the developed CMT well describes the reflected and transmitted fields in a relatively narrow  $x$  range, in which only one eigenmode is excited. For example, if we would consider greater values of  $x$  in Fig. 4, the peaks and dips corresponding to the excitation of higher-order Fabry-Pérot modes would appear in the plots obtained using the local uniform approximation and the RCWA. Each of these peaks can also be described using the CMT by taking different  $k$  values in Eq. (39).

To demonstrate that the considered structure indeed works as an LVF, we repeated the simulations for several wavelengths ranging from 750 nm to 850 nm. The results are presented in Fig. 5, which shows that the CMT predictions are in good agreement with the RCWA results. In particular, the CMT accurately reproduces the spatial shift in the resonant peak position appearing with the change in the wavelength. Note that the CMT parameters, which were used to calculate the plots in Figs. 5(c) and 5(f), were the same as presented above since the angular frequency  $\omega$  is explicitly present in the derived CMT equation (40). Therefore, we demonstrate that

the developed CMT can be used to describe compact linear variable filters with the wedge angle being not negligibly small. The CMT not only reproduces the secondary peaks appearing near the main one, but also enables obtaining accurate estimates for the amplitudes of the electromagnetic field above and below the structure.

## VI. CONCLUSION

In the present work, we developed and numerically verified two formulations of the coupled-mode theory for a Fabry-Pérot resonator in a symmetric environment. In the frequency domain, the CMT allows one to obtain simple rational approximations for the transmission and reflection coefficients as functions of angular frequency  $\omega$  and in-plane wave number  $k_x$ . In the “spatiotemporal” domain, the CMT is written as a partial differential equation. Making the coefficients of this equation not constant, but spatially dependent allowed us to apply the developed theory to a linear variable filter comprising two Bragg mirrors separated by a wedged defect layer. We demonstrated that the CMT accurately describes the optical properties of the LVF and is significantly less demanding in terms of the computation resources as compared to rigorous electromagnetic simulations. This makes the developed CMT an efficient tool for the design and analysis of linear variable filters.

The developed theory can be applied to a wider range of structures having different claddings instead of the multilayer ones, e.g., subwavelength high-contrast gratings. Even more importantly, one can define an arbitrary thickness variation law  $h(x)$  in the CMT instead of a linear one. This will, in particular, enable describing variable filters with nonlinear  $\lambda(x)$  dependence and compact resonators with finite transverse dimensions. Finally, it is worth noting that while the developed CMT is valid in the vicinity of  $k_x = 0$  (at near-normal incidence), even a simpler theory can be constructed in the case of oblique incidence, in which not a hyperbolic, but a linear dispersion law of the eigenmodes should be assumed, resulting in a first-order PDE.

### ACKNOWLEDGMENTS

This work was funded by the Russian Science Foundation (Grant No. 22-12-00120, development of the CMT and LVF investigation), and performed within the state assignment of the NRC ‘‘Kurchatov Institute’’ (implementation of the simulation software).

### APPENDIX A: HERMITIAN UNITARY APPROXIMATION FOR $\xi$

Here, we derive a rational approximation for the function  $\xi(\omega, k_x)$  [Eq. (4)] in the vicinity of the point  $k_x = 0$ ,  $\omega = \omega_0$ , where  $\omega_0$  is given by Eq. (34). The sought-for approximation has to be unitary [ $|\xi(\omega, k_x)|^2 = 1$ ] and Hermitian [ $\xi(-\omega, k_x) = \xi(\omega, k_x)^*$ ].

Let us first consider the case when  $k - m$  in Eq. (34) is an odd number. To obtain an approximation in this case, we note that  $|\xi|^2 = 1$  implies  $\xi = (\xi + 1)/(\xi^* + 1)$ . Then, we express  $\xi$  in terms of its real and imaginary parts and, after simple transformations, we obtain

$$\xi(\omega, k_x) = \frac{\kappa(q, k_x) + i\omega}{\kappa(q, k_x) - i\omega}, \quad (\text{A1})$$

where  $q = \omega^2$  and  $\kappa(q, k_x) = \sqrt{q}(\text{Re } \xi + 1)/\text{Im } \xi = \sqrt{q} \cot\{\frac{1}{2}\sqrt{qn^2c^{-2} - k_x^2}\}$ . Then, we replace  $\kappa(q, k_x)$  with its Taylor approximation at  $(q, k_x) = (\omega_0^2, 0)$  containing only the constant term, which is zero, the  $q$  term, and the  $k_x^2$  term:

$$\kappa(q, k_x) \approx \frac{nh}{4c} \left[ \frac{c^2}{n^2} k_x^2 - (q - \omega_0^2) \right].$$

Substituting this expression into Eq. (A1) gives the following approximation for  $\xi$ :

$$\xi(\omega, k_x) \approx \frac{v_g^2 k_x^2 - (\omega^2 - \omega_0^2) + \frac{4ic}{nh} \omega}{v_g^2 k_x^2 - (\omega^2 - \omega_0^2) - \frac{4ic}{nh} \omega}, \quad (\text{A2})$$

which is valid for odd values of  $k - m$ .

To obtain the approximation for even values of  $k - m$ , we note that  $\xi = -(\xi - 1)/(\xi^* - 1)$  and after similar steps, we

arrive at the same Eq. (A2) with the only difference being the minus sign before the fraction.

Bringing these two approximations together, we obtain the sought-for unitary Hermitian approximation presented in Eq. (35). To conclude this Appendix, let us note that the obtained approximation is similar to the Chisholm approximant, which provides a rational approximation for two-variable functions [38].

### APPENDIX B: CMT COEFFICIENTS FOR DISPERSIVE INTERFACES

Here, we show how the CMT can be reformulated to take into account the fact that the elements of the scattering matrix  $\mathbf{S}$  of the interfaces depend on  $\omega$  and  $k_x$ . We will take into account linear dependence on  $\omega$  and, due to symmetry, quadratic dependence on  $k_x$ . In this case, as we will demonstrate, the form of the CMT will remain the same and only the values of the coefficients will change. We note that such an approach (redefining the CMT parameters to take into account various additional effects) is widely used in CMT-like theories [1].

In the main part of the article, we obtained the CMT by replacing  $\xi$  with its approximation. Here, we use a different approach for finding the CMT parameters. For the symmetric excitation case, we use Eq. (2) to rewrite Eq. (11) in the following form:

$$R_s = -e^{i\phi} \frac{[(r_2\xi - 1)/\sqrt{r_2\xi}]^*}{(r_2\xi - 1)/\sqrt{r_2\xi}}, \quad (\text{B1})$$

where the numerator is the complex conjugate of the denominator. We note that  $r_2$  and  $\xi$  depend on  $\omega$  and  $k_x$ . Now, we consider the denominator as a function of  $q = \omega^2$  and  $k_x$  and replace it with Taylor series containing only the constant term, the  $q$  term and the  $k_x^2$  term. Comparing the obtained result with Eq. (24) allows one to find the following updated values of the CMT parameters:

$$\gamma = \frac{4c}{nh - \text{cir}_\omega} \times \frac{1 - |r_0|}{1 + |r_0|}, \quad (\text{B2})$$

$$v_g^2 = \frac{c}{n} \times \frac{ch + n\omega_0 i r_{k2}}{nh - \text{cir}_\omega}, \quad (\text{B3})$$

where  $r_0 = r_2(\omega_0, 0)$ ,  $r_\omega = r_2^{(1,0)}(\omega_0, 0)/r_0$ , and  $r_{k2} = r_2^{(0,2)}(\omega_0, 0)/r_0$ .

The obtained expressions for  $\gamma$  and  $v_g$  take into account the  $\omega$  and  $k_x$  dependence of the interface reflection and transmission coefficients. Importantly, for the considered dielectric PSBGs, the logarithmic derivatives  $r_\omega$  and  $r_{k2}$  can be assumed imaginary numbers, therefore, the quantities  $\gamma$  and  $v_g$  are real numbers. One can similarly show that for the case of an antisymmetric excitation, Eqs. (B2) and (B3) also hold true.

- [1] H. A. Haus, *Waves and Fields in Optoelectronics* (Prentice Hall, Hoboken, NJ, 1984).  
 [2] B. E. Little, S. T. Chu, H. A. Haus, J. Foresi, and J.-P. Laine, Microring resonator channel dropping filters, *J. Lightwave Technol.* **15**, 998 (1997).

- [3] S. Fan, W. Suh, and J. D. Joannopoulos, Temporal coupled-mode theory for the Fano resonance in optical resonators, *J. Opt. Soc. Am. A* **20**, 569 (2003).  
 [4] A. Yariv, Coupled-mode theory for guided-wave optics, *IEEE J. Quantum Electron.* **9**, 919 (1973).

- [5] H. J. W. M. Hoekstra, Coupled mode theory for resonant excitation of waveguiding structures, *Opt. Quant. Electron.* **32**, 735 (2000).
- [6] Z. Ruan, H. Wu, M. Qiu, and S. Fan, Spatial control of surface plasmon polariton excitation at planar metal surface, *Opt. Lett.* **39**, 3587 (2014).
- [7] D. V. Nesterenko, S. Hayashi, and V. Soifer, *Ab initio* spatial coupled-mode theory of Fano resonances in optical responses of multilayer interference resonators, *Phys. Rev. A* **106**, 023507 (2022).
- [8] V. R. Shteeman, I. Nusinsky, and A. A. Hardy, Time-dependent coupled mode analysis of parallel waveguides, *J. Opt. Soc. Am. B* **27**, 735 (2010).
- [9] V. Shteeman and A. A. Hardy, Analysis of advanced photonic devices with time-dependent coupled mode equations, *Opt. Eng.* **51**, 054001 (2012).
- [10] B. Dana, L. Lobachinsky, and A. Bahabad, Spatiotemporal coupled-mode theory in dispersive media under a dynamic modulation, *Opt. Commun.* **324**, 165 (2014).
- [11] Y. Sivan, S. Rozenberg, and A. Halstuch, Coupled-mode theory for electromagnetic pulse propagation in dispersive media undergoing a spatiotemporal perturbation: Exact derivation, numerical validation, and peculiar wave mixing, *Phys. Rev. B* **93**, 144303 (2016).
- [12] D. A. Bykov and L. L. Doskolovich, Spatiotemporal coupled-mode theory of guided-mode resonant gratings, *Opt. Express* **23**, 19234 (2015).
- [13] D. A. Bykov, E. A. Bezus, and L. L. Doskolovich, From coupled plane waves to the coupled-mode theory of guided-mode resonant gratings, *Photon. Nanostr. Fund. Appl.* **56**, 101167 (2023).
- [14] Z. Dong, X. Chen, and L. Yuan, Spatiotemporal coupled-mode equations for arbitrary pulse transformation, *Phys. Rev. Res.* **5**, 043150 (2023).
- [15] A. Overvig, S. A. Mann, and A. Alu, Spatio-temporal coupled mode theory for nonlocal metasurfaces, *Light Sci. Appl.* **13**, 28 (2024).
- [16] R. R. McLeod and T. Honda, Improving the spectral resolution of wedged etalons and linear variable filters with incidence angle, *Opt. Lett.* **30**, 2647 (2005).
- [17] A. Emadi, H. Wu, S. Grabarnik, G. De Graaf, K. Hedsten, P. Enoksson, J. Correia, and R. Wolffenbuttel, Fabrication and characterization of IC-compatible linear variable optical filters with application in a micro-spectrometer, *Sens. Actuators A: Phys.* **162**, 400 (2010).
- [18] A. Emadi, H. Wu, G. de Graaf, and R. Wolffenbuttel, Design and implementation of a sub-nm resolution microspectrometer based on a linear-variable optical filter, *Opt. Express* **20**, 489 (2012).
- [19] A. Emadi, H. Wu, G. de Graaf, P. Enoksson, J. H. Correia, and R. Wolffenbuttel, Linear variable optical filter-based ultraviolet microspectrometer, *Appl. Opt.* **51**, 4308 (2012).
- [20] X. Yu, Q. Lu, H. Gao, and H. Ding, Development of a handheld spectrometer based on a linear variable filter and a complementary metal-oxide-semiconductor detector for measuring the internal quality of fruit, *J. Near Infrared Spectrosc.* **24**, 69 (2016).
- [21] M. Ghaderi, N. P. Ayerden, A. Emadi, P. Enoksson, J. H. Correia, G. de Graaf, and R. F. Wolffenbuttel, Design, fabrication and characterization of infrared LVOFs for measuring gas composition, *J. Micromech. Microeng.* **24**, 084001 (2014).
- [22] N. P. Ayerden, G. de Graaf, and R. F. Wolffenbuttel, Compact gas cell integrated with a linear variable optical filter, *Opt. Express* **24**, 2981 (2016).
- [23] A. Piegari and J. Bulir, Variable narrowband transmission filters with a wide rejection band for spectrometry, *Appl. Opt.* **45**, 3768 (2006).
- [24] A. Piegari, J. Bulir, and A. K. Sytchkova, Variable narrow-band transmission filters for spectrometry from space. 2. Fabrication process, *Appl. Opt.* **47**, C151 (2008).
- [25] I. G. E. Renhorn, D. Bergström, J. Hedborg, D. Letalick, and S. Möller, High spatial resolution hyperspectral camera based on a linear variable filter, *Opt. Eng.* **55**, 114105 (2016).
- [26] M. G. Moharam, E. B. Grann, D. A. Pommert, and T. K. Gaylord, Formulation for stable and efficient implementation of the rigorous coupled-wave analysis of binary gratings, *J. Opt. Soc. Am. A* **12**, 1068 (1995).
- [27] U. Fano, Effects of configuration interaction on intensities and phase shifts, *Phys. Rev.* **124**, 1866 (1961).
- [28] D. V. Nesterenko, S. Hayashi, and Z. Sekkat, Asymmetric surface plasmon resonances revisited as Fano resonances, *Phys. Rev. B* **97**, 235437 (2018).
- [29] N. V. Golovastikov, D. A. Bykov, L. L. Doskolovich, and V. A. Soifer, Analytical description of 3D optical pulse diffraction by a phase-shifted Bragg grating, *Opt. Express* **24**, 18828 (2016).
- [30] N. V. Golovastikov, D. A. Bykov, L. L. Doskolovich, and V. A. Soifer, Spatiotemporal optical pulse transformation by a resonant diffraction grating, *J. Exp. Theor. Phys.* **121**, 785 (2015).
- [31] H. M. Nussenzveig, *Causality and Dispersion Relations* (Academic, New York, 1972).
- [32] V. Grigoriev, S. Varault, G. Boudarham, B. Stout, J. Wenger, and N. Bonod, Singular analysis of Fano resonances in plasmonic nanostructures, *Phys. Rev. A* **88**, 063805 (2013).
- [33] D. A. Bykov and L. L. Doskolovich,  $\omega-k_x$  Fano line shape in photonic crystal slabs, *Phys. Rev. A* **92**, 013845 (2015).
- [34] L. Li, Formulation and comparison of two recursive matrix algorithms for modeling layered diffraction gratings, *J. Opt. Soc. Am. A* **13**, 1024 (1996).
- [35] K. Kinoshita, Numerical evaluation of the intensity curve of a multiple-beam Fizeau fringe, *J. Phys. Soc. Jpn.* **8**, 219 (1953).
- [36] Y. H. Meyer, Fringe shape with an interferential wedge, *J. Opt. Soc. Am.* **71**, 1255 (1981).
- [37] T. T. Kajava, H. M. Lauranto, and A. T. Friberg, Interference pattern of the Fizeau interferometer, *J. Opt. Soc. Am. A* **11**, 2045 (1994).
- [38] J. Chisholm, Rational approximants defined from double power series, *Math. Comp.* **27**, 841 (1973).